Supporting Information

Fine-tuning the Pore Environment of Isoreticular Metal-Organic Frameworks through Installing Functional Sites for Boosting C_2H_6/C_2H_4 Separation

Gang-Ding Wang[a], Yong-Zhi Li[c],* Rajamani Krishna,[b] Zhi-Zhu Yan [a], Lei Hou[a],* Yao-Yu Wang[a], and Zhonghua Zhu[c]

[a]Key Laboratory of Synthetic and Natural Functional Molecule of the Ministry of Education, Shaanxi Key Laboratory of Physico-Inorganic Chemistry, College of Chemistry & Materials Science, Northwest University, Xi'an 710069, P. R. China.

[b]Van 't Hoff Institute for Molecular Sciences University of Amsterdam Science Park 904, 1098 XH Amsterdam, The Netherlands.

[c]School of Materials and Physics, China University of Mining and Technology Xuzhou 221116, P. R. China.

[d]School of Chemical Engineering, The University of Queensland, Brisbane 4072, Australia.

*To whom correspondence should be addressed. E-mail: Lyz2021@cumt.edu.cn (Yong-Zhi Li); lhou2009@nwu.edu.cn (Lei Hou).

Materials and general methods

All solvents and organic ligand for synthesis were purchased commercially. Elemental analyses of C, H, and N were determined with a Perkin-Elmer 2400C elemental analyzer. Thermalgravimetric analyses (TGA) were carried out in a nitrogen stream using a Netzsch TG209F3 equipment at a heating rate of 10 °C min^{-1}. Single crystal diffraction data were collected on a Bruker SMART APEX II CCD single crystal diffractometer. Gas adsorption measurements were performed with an automatic volumetric sorption apparatus (Micrometrics ASAP 2020M), in which the sample was activated by immersing in CH_2Cl_2 for 72 hours and then heating at 393 K under vacuum for 4 hours. Water sorption was collected by Quantachrome Vstar vapor adsorption equipment. Breakthrough experiments were performed on a Quantachrome dynaSorb BT equipments.

X-ray crystallography

A Bruker Smart Apex II CCD detector was used to collect the single crystal data at 180(2) or 174(2) K using Mo Kα radiation (λ = 0.71073 Å). The structure was solved by direct methods and refined by full-matrix least-squares refinement based on F2 with the SHELXTL program. The non-hydrogen atoms were refined anisotropically with the hydrogen atoms added at their geometrically ideal positions and refined isotropically. As the disordered solvent molecules in the structure cannot be located, the SQUEEZE routine of Platon program was applied in refining. The formula of complex was got by the single crystal analysis together with elemental microanalyses and TGA data. Relevant crystallographic results were listed in Table S5. Selected bond lengths and angles were provided in Table S6.

Fitting of unary isotherm data

The unary isotherms for C_2H_6, and C_2H_4, measured at two different temperatures 273 K, and 298 K in MAF-X10(F), MAF-X10(Cl), MAF-X10(Me), and MAF-X10 were fitted with excellent accuracy using the 1-site Langmuir-Freundlich model:

$$q = \frac{q_{sat} b p^{v}}{1 + b p^{v}} \qquad \text{(S1)}$$

In eq (S1), the Langmuir-Freundlich parameter b is temperature dependent

$$b = b_0 \exp\left(\frac{E}{RT}\right) \quad \text{(S2)}$$

In eq (S2), E is the energy parameter. The unary isotherm fit parameters are provided in Table S1, Table S2, Table S3, and Table S4,

Isosteric heat of adsorption

The isosteric heat of adsorption, Q_{st}, is defined as

$$Q_{st} = -RT^2\left(\frac{\partial \ln p}{\partial T}\right)_q \quad \text{(S3)}$$

where, the derivative in the right member of eq (S3) is determined at constant adsorbate loading, q. the derivative was determined by analytic differentiation of the combination of eq (S1), eq (S2), and eq (S3).

Table S1. 1-site Langmuir-Freundlich fits for C_2H_6 and C_2H_4 in MAF-X10(F).

	q_{sat} / mol/kg	b_0 / Pa^{-1}	E / kJ mol^{-1}	ν
C_2H_6	14	3.322E-10	24.9	1
C_2H_4	13.5	6.665E-10	21.7	1

Table S2. 1-site Langmuir-Freundlich fits for C_2H_6 and C_2H_4 in MAF-X10(Cl).

	q_{sat} / mol/kg	b_0 / Pa^{-1}	E / kJ mol^{-1}	ν
C_2H_6	11.5	3.081E-11	28	1.12
C_2H_4	14.5	2.847E-10	23.5	1

Table S3. 1-site Langmuir-Freundlich fits for C_2H_6 and C_2H_4 in MAF-X10(Me).

	q_{sat} / mol/kg	b_0 / Pa^{-1}	E / kJ mol^{-1}	ν
C_2H_6	10.7	2.589E-11	29	1.085
C_2H_4	13	8.232E-10	21.2	1

Table S4. 1-site Langmuir-Freundlich fits for C_2H_6 and C_2H_4 in MAF-X10.

	$\frac{q_{sat}}{\text{mol/kg}}$	$\frac{b_0}{\text{Pa}^{-1}}$	$\frac{E}{\text{kJ mol}^{-1}}$	ν
C_2H_6	14.7	3.950E-10	23.4	1
C_2H_4	12.8	4.449E-10	22.4	1

Gas selectivity prediction via IAST

The experimental isotherm data for pure C_2H_4 and C_2H_6 were fitted using a dual Langmuir-Freundlich (L-F) model:

$$q = \frac{a_1 * b_1 * P^{c_1}}{1 + b_1 * P^{c_1}} + \frac{a_2 * b_2 * P^{c_2}}{1 + b_2 * P^{c_2}}$$

Where q and p are adsorbed amounts and the pressure of component i, respectively.

The adsorption selectivities for binary mixtures defined by

$$S_{i/j} = \frac{x_i * y_j}{x_j * y_i}$$

were respectively calculated using the Ideal Adsorption Solution Theory (IAST). Where *xi* is the mole fraction of component *i* in the adsorbed phase and *yi* is the mole fraction of component *i* in the bulk.

Breakthrough experiments

The breakthrough experiment was performed on the Quantachrome dynaSorb BT equipments at 298 K and 1 bar with an equal volume of mixed gas (gas A: gas B: Ar = 5% : 5% : 90%, Ar as the carrier gas, flow rate = 5 mL min^{-1}). The activated MOFs (about 0.65 g) were filled into a packed column of ϕ 4.2×80 mm, and then the packed column was washed with Ar at a rate of 7 mL min^{-1} at 333 K for 35 minutes to further activate the samples. Between two breakthrough experiments, the adsorbent was regenerated by Ar flow of 7 mL min^{-1} for 35 min at 333 K to guarantee a complete removal of the adsorbed gases.

Molecular simulations

Grand canonical Monte Carlo (GCMC) simulations were performed for the gas adsorption in the framework by the Sorption module of Material Studio (Accelrys. Materials Studio Getting Started). The framework was considered to be rigid, and the optimized gas molecules were used. The partial charges for atoms of the framework were derived from QEq method

and QEq neutral 1.0 parameter. One unit cell was used during the simulations. The interaction energies between the gas molecules and framework were computed through the Coulomb and Lennard-Jones 6-12 (LJ) potentials. All parameters for the atoms were modeled with the universal force field (UFF) embedded in the MS modeling package. A cutoff distance of 12.5 Å was used for LJ interactions, and the Coulombic interactions were calculated by using Ewald summation. For each run, the 5×10^6 maximum loading steps, 5×10^6 production steps were employed.

Transient breakthrough simulations *vs* experiments with inert gas

The transient breakthrough experiments were conducted with mass of MAF-X10(F), MAF-X10(Cl), MAF-X10(Me), and MAF-X10 m_{ads}= 0.65 g; length of packed bed, L = 80 mm; inner diameter of packed bed= 4.2 mm. The mixtures examined were: C_2H_6/C_2H_4/Ar mixtures (5/5/90, 1/9/90, and 1/15/84, v/v/v) with Ar as the carrier gas, and a total flow rate of 5 mL min^{-1} (298 K, 100 kPa).

Transient breakthrough simulations were carried out for the exact same set of operating conditions as in the above mentioned experiments, using the methodology described in earlier publications.[1-6] In these simulations, intra-crystalline diffusion influences are ignored. For MAF-X10(F), MAF-X10(Cl), and MAF-X10, there is good match between the experiments and simulations. For MAF-X10(Me), the experiments show better separation performance than anticipated by the breakthrough simulations.

Transient breakthrough simulations without inert gas

Having established the accuracy of the transient breakthrough simulations, a set of simulations were carried out without inert gas in a fixed bed packed with MAF-X10(F), MAF-X10(Cl), MAF-X10(Me), and MAF-X10 m_{ads} = 0.65 g; length of packed bed, L = 80 mm; inner diameter of packed bed= 4.2 mm. The total pressure is 100 kPa, and two different temperatures were used: 298 K. The following mixtures were simulated.

50/50 C_2H_6(1)/C_2H_4(2) mixtures

10/90 C_2H_6(1)/C_2H_4(2) mixtures

6.25/97.5 C_2H_6(1)/C_2H_4(2) mixtures

The breakthrough data are presented in terms of the dimensionless concentrations at the exit

of the fixed bed, $\frac{c_A}{c_{A0}}$, as function of the modified time parameter $\frac{(Q_0 = flow\ rate\ mL\ min^{-1}) \times (time\ in\ min)}{(g\ MOF\ packed\ in\ tube)} = \frac{Q_0 t}{m_{ads}} = mL\ g^{-1}$.

Notation

b	Langmuir-Freundlich constant, Pa^{-v}
E	energy parameter, J mol^{-1}
L	length of packed bed adsorber, m
m_{ads}	mass of adsorbent packed in fixed bed, kg
p_i	partial pressure of species i, Pa
q_i	component molar loading of species i, mol kg^{-1}
q_{sat}	saturation loading, mol kg^{-1}
Q_0	volumetric flow rate of gas mixture entering fixed bed, $m^3\ s^{-1}$
Q_{st}	isosteric heat of adsorption, J mol^{-1}
T	absolute temperature, K

Greek letters

v	Freundlich exponent, dimensionless
ρ	framework density, kg m^{-3}

Molecular structure	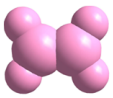				
Molecular formula	**Molecular Dimension (Å)**			**Kinetic diameter (Å)**	**Polari × 10^{-25} (cm^{-3})**	**Boiling point(K)**
	X	***Y***	***Z***			
C_2H_4	3.28	4.18	4.84	4.16	42.5	169.4
C_2H_6	3.81	4.08	4.82	4.44	44.3-44.7	184.6

Scheme S1. Structures and physical properties of C_2H_4 and C_2H_6.

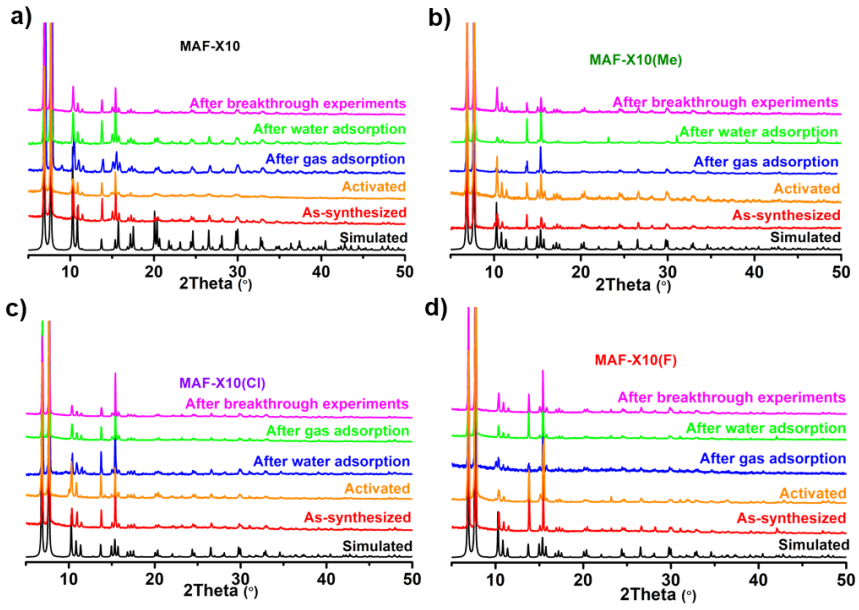

Figure S1. PXRD patterns of simulated from crystal structure, as-synthesized, activated, after water adsorption, gas adsorption, and breakthrough experiment samples for a) MAF-X10; b) MAF-X10(Me); c) MAF-X10(Cl); d) MAF-X10(F).

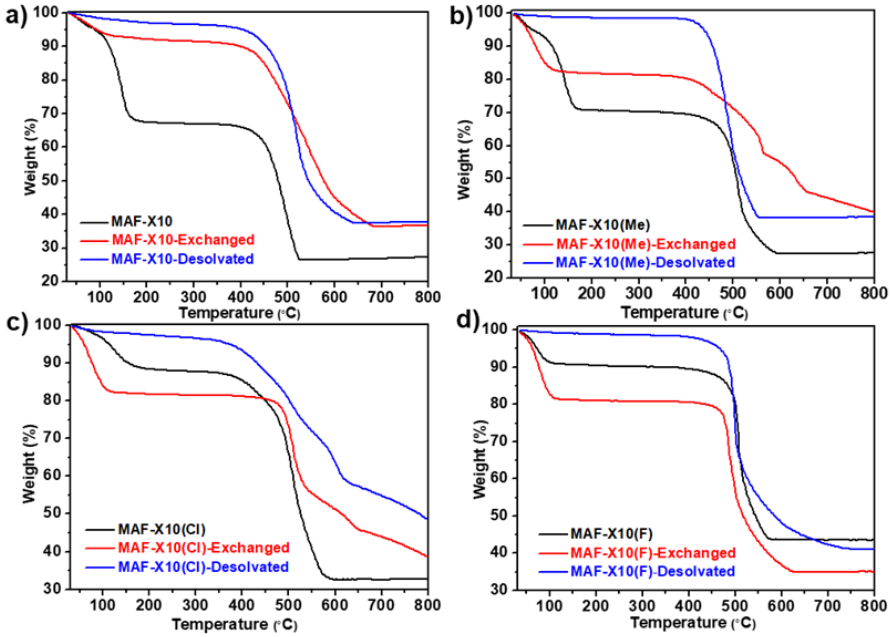

Figure S2. TGA curves of as-synthesized and dichloromethane-exchanged samples of a) MAF-X10; b) MAF-X10(Me); c) MAF-X10(Cl); d) MAF-X10(F).

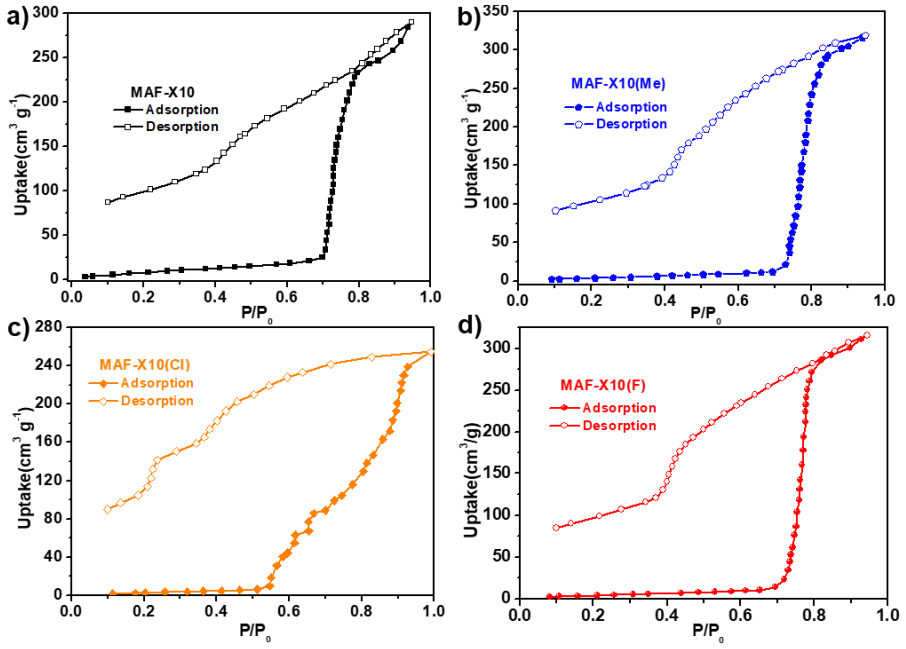

Figure S3. Water vapor adsorption and desorption isotherm of a) MAF-X10; b) MAF-X10(Me); c) MAF-X10(Cl); d) MAF-X10(F) at 298 K.

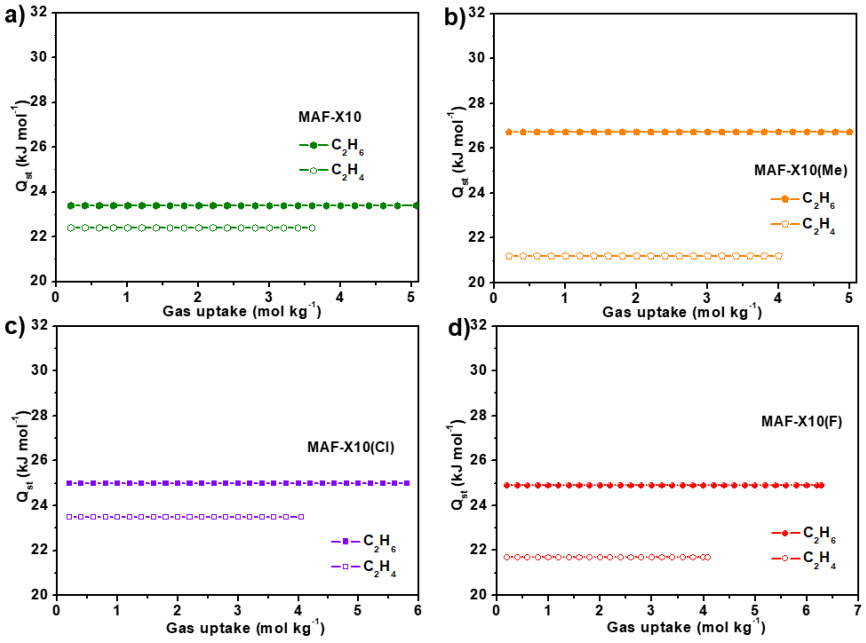

Figure S4.a) Adsorption enthalpies (Q_{st}) of C_2H_6 (solid) and C_2H_4 (hollow) for MAF-X10; b) adsorption enthalpies (Q_{st}) of C_2H_6 (solid) and C_2H_4 (hollow) for MAF-X10(Me); c) adsorption enthalpies (Q_{st}) of C_2H_6 (solid) and C_2H_4 (hollow) for MAF-X10(Cl); d) adsorption enthalpies (Q_{st}) of C_2H_6 (solid) and C_2H_4 (hollow) for MAF-X10(F).

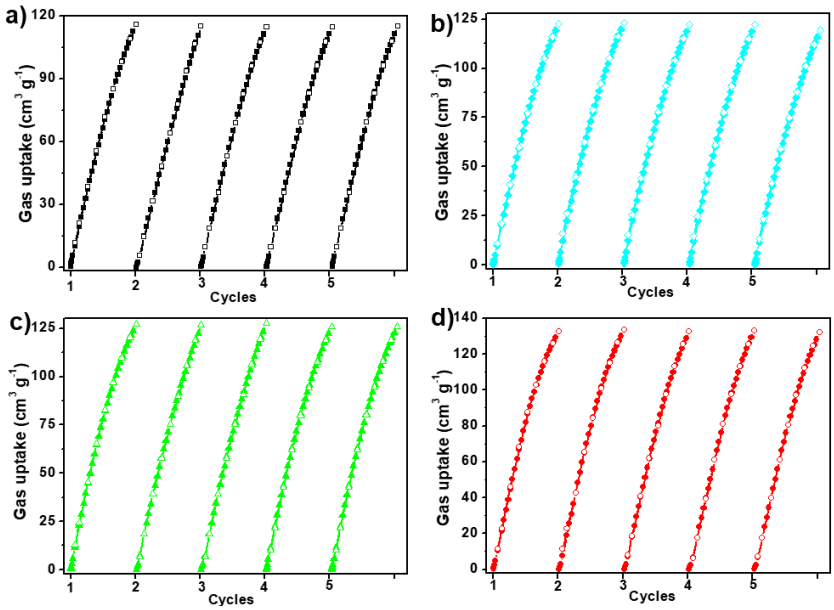

Figure S5. Cycles of C_2H_6 adsorption for a) MAF-X10; b) MAF-X10(Me), c) MAF-X10(Cl) and d) MAF-X10(F) at 298 K.

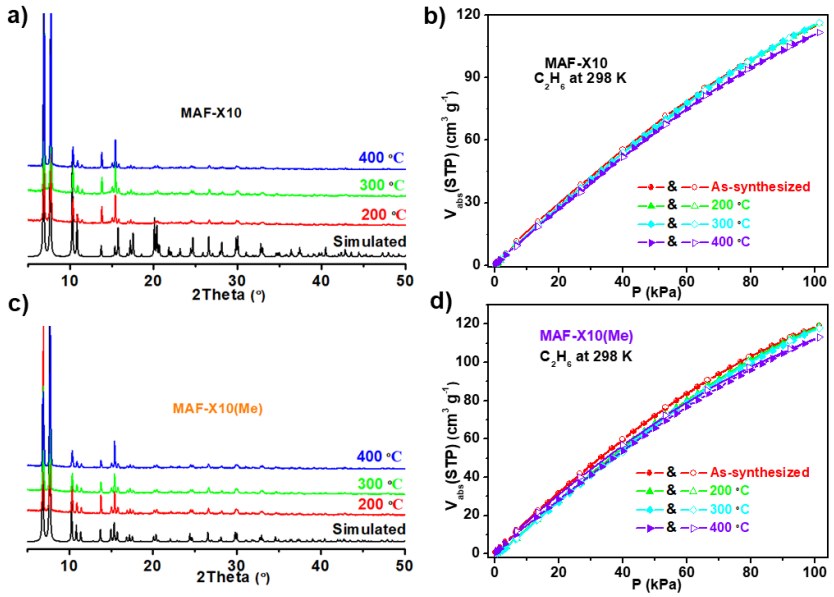

Figure S6. a) and b) PXRD patterns of MAF-X10 treated under different temperatures, C_2H_6 sorption isotherms at 298 K of MAF-X10 treated under different temperature; c) and d) PXRD patterns of MAF-X10(Me) treated under different temperatures, C_2H_6 sorption isotherms at 298 K of MAF-X10(Me) treated under different temperature.

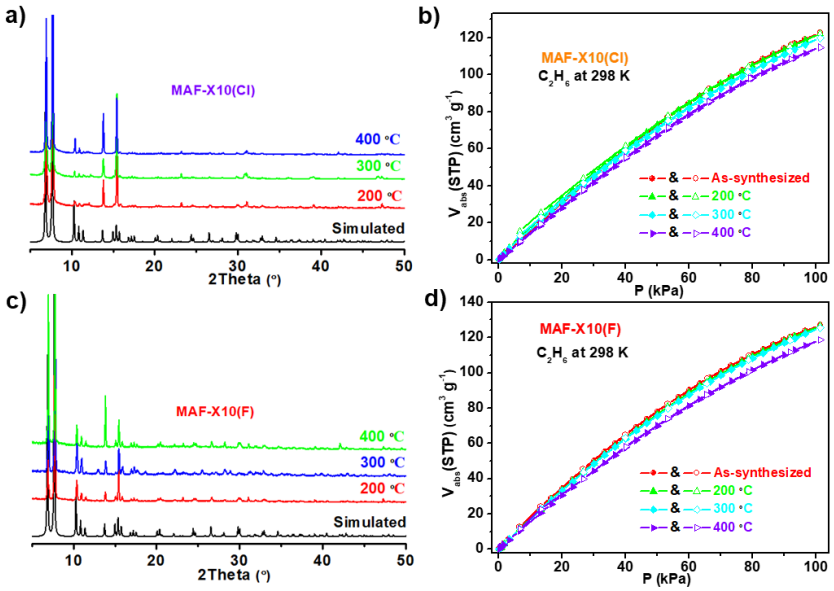

Figure S7. a) and b) PXRD patterns of MAF-X10(Cl) treated under different temperatures, C_2H_6 sorption isotherms at 298 K of MAF-X10(Cl) treated under different temperature; c) and d) PXRD patterns of MAF-X10(F) treated under different temperatures, C_2H_6 sorption isotherms at 298 K of MAF-X10(F) treated under different temperature.

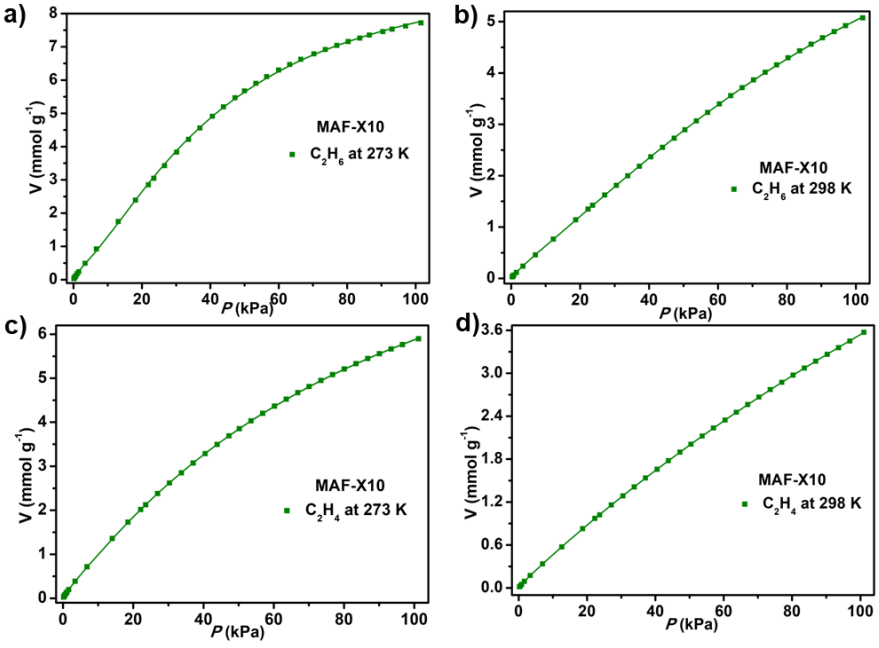

Figure S8. a) and b) C_2H_6 adsorption isotherms of MAF-X10 with fitted by dual L-F model at 273 K (a) and 298 K (b), 273 K: a1 = 9.40912, b1 = 0.00364, c1 = 1.50211, a2 = 0.33029, b2 = 0.79455, c2 = 1.44408, Chi^2 = 0.00101, R^2 = 0.99989; 298 K: a1 = 9.94983, b1 = 0.00145, c1 = 1.38093, a2 = 0.53361, b2 = 0.14091, c2 = 0.96028, Chi^2 = 0.00005, R^2 =

0.99998; c) and d) C_2H_4 adsorption isotherms of MAF-X10 with fitted by dual L-F model at 273 K (c) and 298 K (d), 273 K: a1 = 10.89243, b1 = 0.00672, c1 = 1.10867, a2 = 0.15068, b2 = 0.63238, c2 = 1.04784, Chi^2 = 0.00003, R^2 = 0.99999; 298 K: a1 = 16.09448, b1 = 0.00262, c1 = 1.01164, a2 = 0.06281, b2 = 0.32365, c2 = 0.86659, Chi^2 = 5.0292E-6, R^2 = 1.

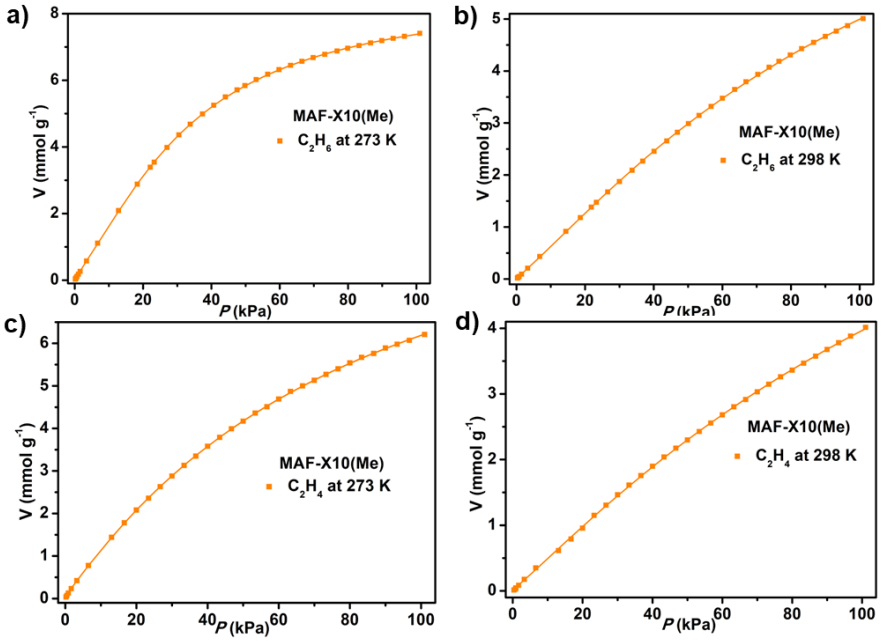

Figure S9. a) and b) C_2H_6 adsorption isotherms of MAF-X10(Me) with fitted by dual L-F model at 273 K (a) and 298 K (b), 273 K: a1 =8.16174, b1 = 0.00546, c1 = 1.49485, a2 = 0.51061, b2 = 0.33046, c2 = 1.23275, Chi^2 = 0.00012, R^2 = 0.99999; 298 K: a1 = 10.48867, b1 = 0.00351, c1 = 1.2003, a2 = 0.07733, b2 = 0.59516, c2 = 1.37423, Chi^2 = 0.0001, R^2 = 0.99997; c) and d) C_2H_4 adsorption isotherms of MAF-X10(Me) with fitted by dual L-F model at 273 K (c) and 298 K (d), 273 K: a1 = 10.8874, b1 = 0.00844, c1 = 1.08571, a2 = 0.13483, b2 = 0.78228, c2 = 1.08874, Chi^2 = 0.0001, R^2 = 0.99998; 298 K: a1 = 10.90779, b1 = 0.00351, c1 = 1.10354, a2 = 0.02684, b2 = 0.35294, c2 = 3.87813, Chi^2 = 0.00019, R^2 = 0.9999.

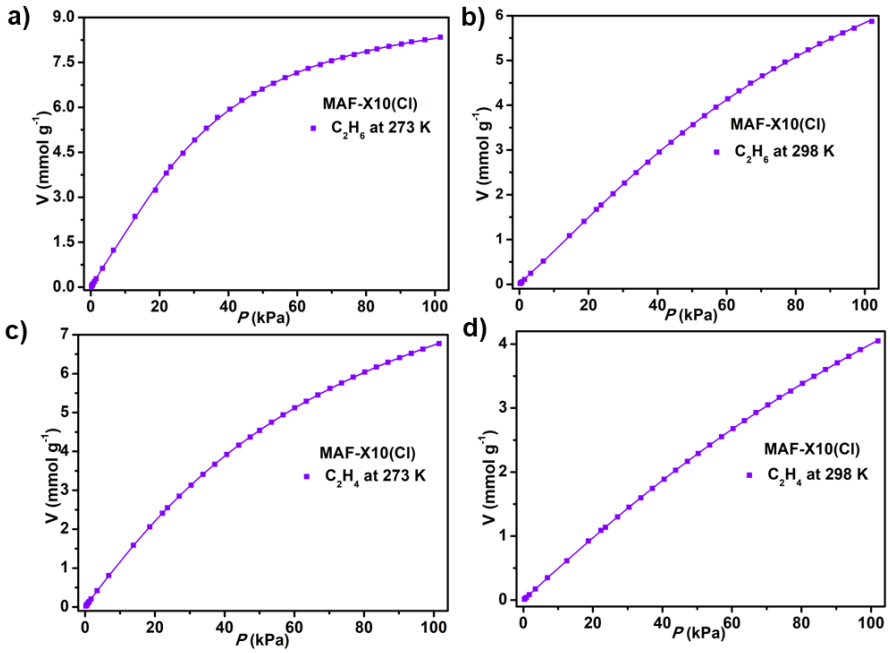

Figure S10. a) and b) C_2H_6 adsorption isotherms of MAF-X10(Cl) with fitted by dual L-F model at 273 K (a) and 298 K (b), 273 K: a1 = 8.85551, b1 = 0.00421, c1 = 1.58066, a2 = 0.69627, b2 = 0.2573, c2 = 1.32337, Chi^2 = 0.00067, R^2 = 0.99994; 298 K: a1 = 10.64733, b1 = 0.00307, c1 = 1.2865, a2 = 0.15369, b2 = 0.38806, c2 = 1.37816, Chi^2 = 0.00016, R^2 = 0.99996; c) and d) C_2H_4 adsorption isotherms of MAF-X10(Cl) with fitted by dual L-F model at 273 K (c) and 298 K (d), 273 K: a1 = 11.21304, b1 = 0.00742, c1 = 1.14242, a2 = 0.13783, b2 = 0.42681, c2 = 1.19246, Chi^2 = 0.00003, R^2 = 1; 298 K: a1 = 12.82673, b1 = 0.00316, c1 = 1.07547, a2 = 0.03242, b2 = 0.43114, c2 = 1.35749, Chi^2 = 0.00002, R^2 = 0.99999.

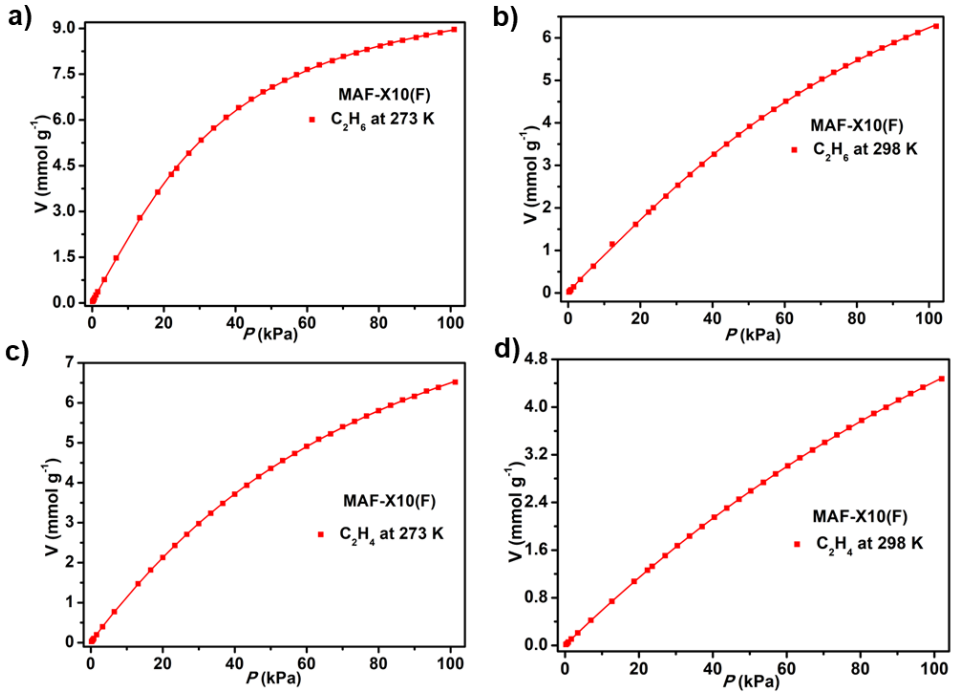

Figure S11. a) and b) C_2H_6 adsorption isotherms of MAF-X10(F) with fitted by dual L-F model at 273 K (a) and 298 K (b), 273 K: a1 = 10.3867, b1 = 0.00887, c1 = 1.35191, a2 = 0.44633, b2 = 0.51986, c2 = 1.10744, Chi^2 = 0.00037, R^2 = 0.99997; 298 K: a1 = 10.93585, b1 = 0.00336, c1 = 1.2755, a2 = 0.28759, b2 = 0.25276, c2 = 1.311, Chi^2 = 0.00035, R^2 = 0.99993; c) and d) C_2H_4 adsorption isotherms of MAF-X10(F) with fitted by dual L-F model at 273 K (c) and 298 K (d), 273 K: a1 = 11.25405, b1 = 0.00763, c1 = 1.11615, a2 = 0.1327, b2 = 0.43408, c2 = 1.28503, Chi^2 = 0.00009, R^2 = 0.99998; 298 K: a1 = 13.36461, b1 = 0.00347, c1 = 1.04621, a2 = 0.0503, b2 = 0.19085, c2 = 1.17644, Chi^2 = 2.8772E-6, R^2 = 1.

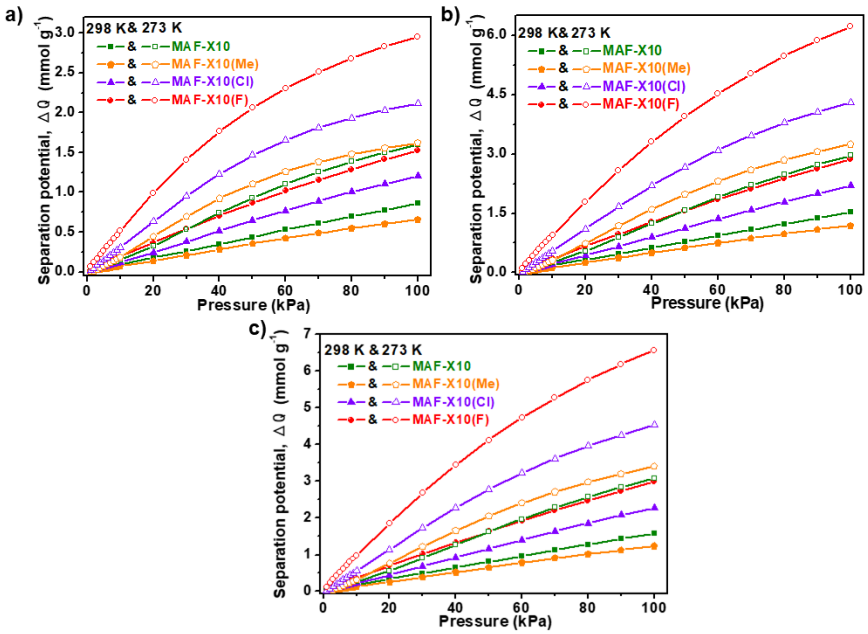

Figure S12. a-c) Separation potential of four MOFs for C_2H_6/C_2H_4 mixtures at 273 and 298 K: a) (v/v; 1/1), b) (v/v; 1/9), c) (v/v; 1/15) (solid curves represent 298 K and hollow curves represent 273 K; olive represent MAF-X10, orange represent MAF-X10(Me), violet represent MAF-X10(Cl) and red represent MAF-X10(F)).

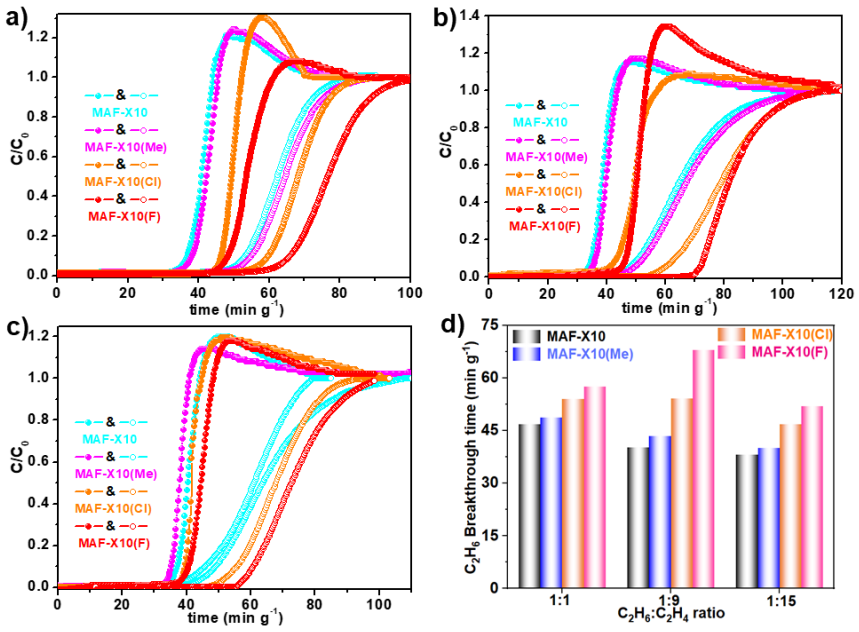

Figure S13. Experimental breakthrough curves for MAF-X10, MAF-X10(Me), MAF-X10(Cl) and MAF-X10(F) at 273 K and 100 kPa, a) (v/v; 5/5), b) (v/v; 1/9), c) (v/v; 1/15); d) C_2H_6 breakthrough time for MAF-X10, -(Me), -(Cl) and -(F) at 273 K.

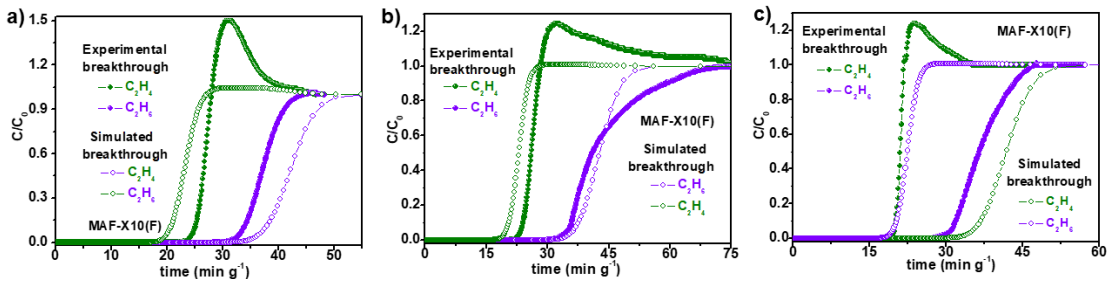

Figure S14. Comparison of the transient breakthrough curves and experimental breakthrough curves for MAF-X10(F) at 298 K: a) C_2H_6/C_2H_4 (5/5) mixtures, b) C_2H_6/C_2H_4 (1/9) mixtures, c) C_2H_6/C_2H_4 (1/15) mixtures.

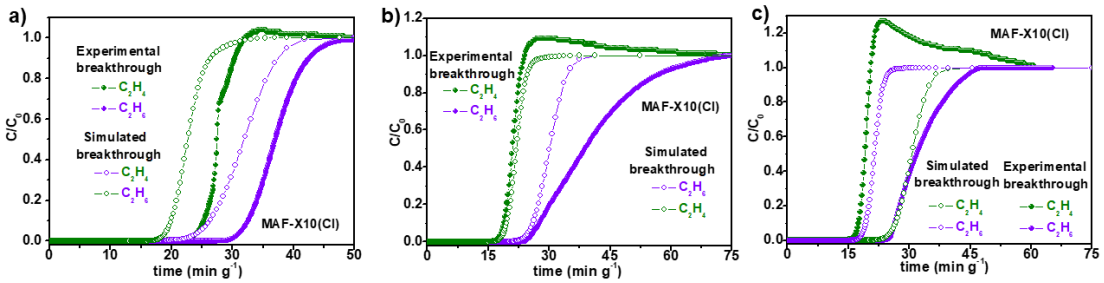

Figure S15. Comparison of the transient breakthrough curves and experimental breakthrough curves for MAF-X10(Cl) at 298 K: a) C_2H_6/C_2H_4 (5/5) mixtures, b) C_2H_6/C_2H_4 (1/9) mixtures, c) C_2H_6/C_2H_4 (1/15) mixtures.

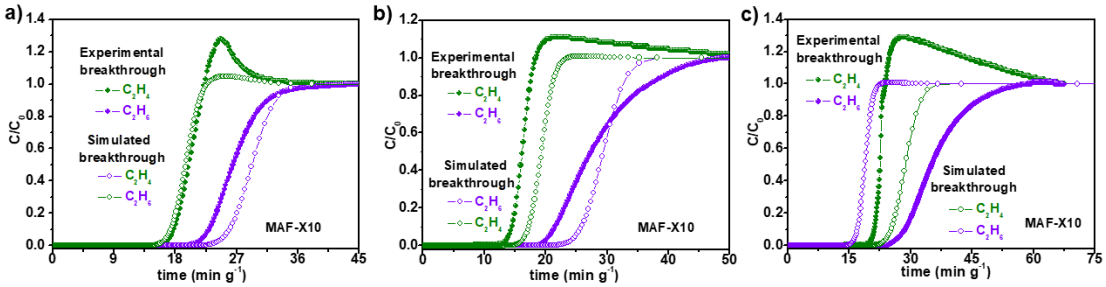

Figure S16. Comparison of the transient breakthrough curves and experimental breakthrough curves for MAF-X10 at 298 K: a) C_2H_6/C_2H_4 (5/5) mixtures, b) C_2H_6/C_2H_4 (1/9) mixtures, c) C_2H_6/C_2H_4 (1/15) mixtures.

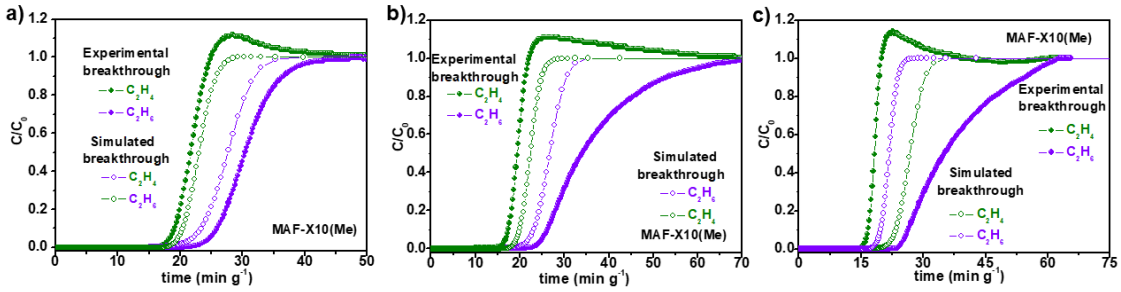

Figure S17. Comparison of the transient breakthrough curves and experimental breakthrough curves for MAF-X10(Me) at 298 K: a) C_2H_6/C_2H_4 (5/5) mixtures, b) C_2H_6/C_2H_4 (1/9) mixtures, c) C_2H_6/C_2H_4 (1/15) mixtures.

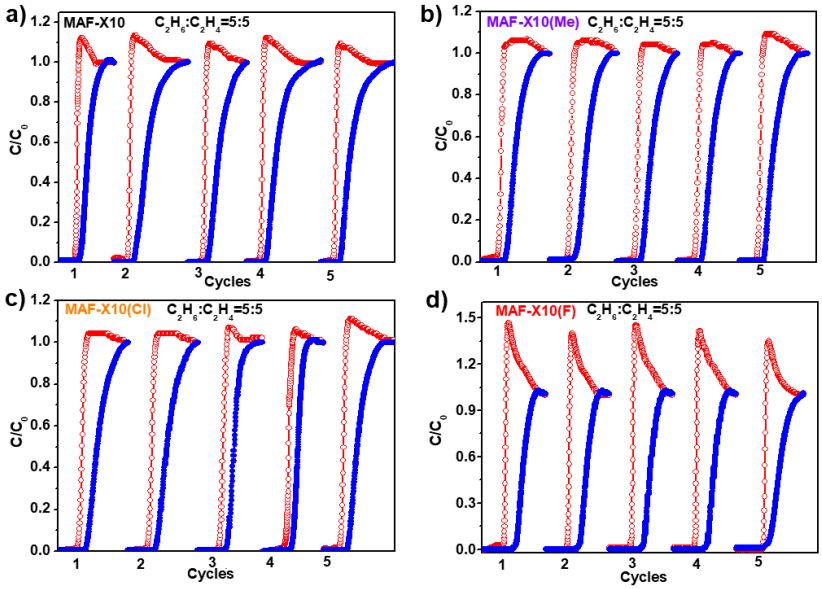

Figure S18. Cycling tests for equimolar C_2H_6/C_2H_4 (v/v; 5/5) mixtures at 298 K a) MAF-X10, b) MAF-X10(Me), c) MAF-X10(Cl), and d) MAF-X10(F).

Table S5. Crystal Data and Structure Refinements for MOFs.

	MAF-X10(Me)	MAF-X10(F)	MAF-X10(Cl)
Chemical formula	$C_{29}H_{30}N_8O_5Zn_4$	$C_{28}H_{27}FN_8O_5Zn_4$	$C_{28}H_{27}ClN_8O_5Zn_4$
Formula weight	832.09	836.05	852.50
T (K)	180(2) K	174(2) K	180(2) K
Crystal system	tetragonal	tetragonal	tetragonal
Space group	$P4_2/mcm$	$P4_2/mcm$	$P4_2/mcm$
a (Å)	11.5296(3)	11.5302(4)	11.5284(3)
b (Å)	11.5296(3)	11.5302(4)	11.5284(3)
c (Å)	25.8084(13)	25.768(2)	25.8176(13)
α (°), β (°), γ (°)	90,90,90	90,90,90	90,90,90
V (Å^3)	3430.8(2)	3425.7(4)	3431.3(2)
Z, $D_{calcd.}$[g·cm^{-3}]	2, 0.805	2, 0.811	2, 0.825
μ (mm^{-1}), Goof	1.406, 1.154	1.410, 1.179	1.444, 1.242
Reflns collected/unique/R_{int}	11324/1720/0.0473	11636/1701/0.07544	21768/1716/0.0438
Theta range for data collection	2.620 to 25.347°	2.620 to 25.366°	2.620 to 25.346°
R_1[a], wR_2[b] [I > 2σ]	0.0534, 0.1216	0.1144, 0.2575	0.0556, 0.1329
R_1[a], wR_2[b] (all data)	0.0580, 0.1235	0.1248, 0.2616	0.0583, 0.1341
CCDC number	2266974	2266975	2266976

[a]$R_1 = \Sigma(|F_o|-|F_c|)/\Sigma|F_o|$. [b]$R_2 = [\Sigma w(F_o^2 - F_c^2)^2/\Sigma w(F_o^2)^2]^{1/2}$.

Table S6. Selected bond lengths [Å] and angles [°] for MOFs.

MAF-X10(Me)					
Zn(1)-O(1)	1.9420(6)	O(1)-Zn(1)-O(2)	109.22(12)	O(1)-Zn(1)-N(1)	99.38(9)
Zn(1)-O(2)	1.961(4)	O(1)-Zn(1)-N(1)#1	99.38(9)	O(2)-Zn(1)-N(1)	112.32(10)
Zn(1)-N(1)#1	1.981(3)	O(2)-Zn(1)-N(1)#1	112.32(10)	N(1)#1-Zn(1)-N(1)	121.72(18)
Zn(1)-N(1)	1.981(3)				
MAF-X10(F)					
Zn(1)-O(2)	1.9418(15)	O(2)-Zn(1)-O(1)	108.9(3)	O(2)-Zn(1)-N(1)#1	99.96(19)
Zn(1)-O(1)	1.954(9)	O(2)-Zn(1)-N(1)	99.96(19)	O(1)-Zn(1)-N(1)#1	112.2(2)
Zn(1)-N(1)	1.978(7)	O(1)-Zn(1)-N(1)	112.2(2)	N(1)-Zn(1)-N(1)#1	121.3(4)
Zn(1)-N(1)#1	1.978(7)				
MAF-X10(F)					
Zn(1)-O(2)	1.9418(15)	O(2)-Zn(1)-O(1)	108.9(3)	O(2)-Zn(1)-N(1)#1	99.96(19)
Zn(1)-O(1)	1.954(9)	O(2)-Zn(1)-N(1)	99.96(19)	O(1)-Zn(1)-N(1)#1	112.2(2)
Zn(1)-N(1)	1.978(7)	O(1)-Zn(1)-N(1)	112.2(2)	N(1)-Zn(1)-N(1)#1	121.3(4)
Zn(1)-N(1)#1	1.978(7)				

Symmetry code: #1 = y, x, z.

Table S7. Adsorption data of MAF-X10 isomorphs and other representative materials.

Materials	C_2H_6 uptake ($cm^3\ g^{-1}$)	C_2H_6/C_2H_4 uptake ratio	Separation Potential ($mmol\ g^{-1}$)	C_2H_6 Q_{st} ($kJ\ mol^{-1}$)	reference
MAF-X10	113.6	1.42	0.856[a]		This work
MAF-X10(Me)	112.2	1.25	0.626[a]		
MAF-X10(Cl)	131.5	1.45	1.203[a]		
MAF-X10(F)	140.5	1.53	1.526[a]		
ZIF-8	56	1.75	0.313[a]	--	7
UPC-613	57.1	1.10	0.456[a]	31.8	8
UiO-67	48.8	1.43	0.465[a]	24.7	9
(Hf)DUT-52	90.0	1.25	1.284[a]	25.6	10
Tb-MOF-76(NH_2)	73.3	1.10	1.10[a]	32.8	11
Tb-MOF-76	68	1.09	0.727[a]	30.9	11
Ni(bdc)(ted)$_{0.5}$	112	1.47	1.132[a]	21	12
PCN-250	116.7	1.21	1.471[a]	23.6	13
MUF-15	105	1.30	1.256[a]	29.2	14
NKCOF-23	60.5	1.18	1.010[a]	24.3	15
CPOC-301	87	1.16	0.480[a]	32.4	16
CPM-733	159.6	1.10	0.850[a]	23.4	17
JNU-2	92	0.55	1.136[a]	29.4	18
MAF-49	38	1.02	1.361[a]	60	19
Fe(O_2)(dobdc)	74.3	1.37	1.739[a]	66.8	20
JNU-6-CH_3	103.7	1.18		24.7	21
HOF-NBDA	89.2	1.9	1.356[b]	23.8	22
Azole-Th-1	100.2	1.24	--	28.6	23

*a = C_2H_6/C_2H_4 (v/v, 50/50), b = C_2H_6/C_2H_4 (v/v, 10/90)

Table S8. Comparisons of C_2H_4 productivities of MAF-X10 isomorphs from the transient breakthrough simulations using C_2H_6/C_2H_4 mixtures as input.

MOFs	Gravimetric productivity ($L\ Kg^{-1}$) with different purities of C_2H_4		C_2H_4 Purity achieved
MAF-X10	C_2H_6/C_2H_4 (50/50,v/v)	5.945	99.96%
	C_2H_6/C_2H_4 (10/90,v/v)	17.685	99.95%
	C_2H_6/C_2H_4 (6.25/93.75,v/v)	19.628	99.96%
MAF-X10(Me)	C_2H_6/C_2H_4 (50/50,v/v)	2.938	99.51%
	C_2H_6/C_2H_4 (10/90,v/v)	4.278	99.95%
	C_2H_6/C_2H_4 (6.25/93.75,v/v)	6.663	99.95%
MAF-X10(Cl)	C_2H_6/C_2H_4 (50/50,v/v)	10.278	99.96%
	C_2H_6/C_2H_4 (10/90,v/v)	25.641	99.96%
	C_2H_6/C_2H_4 (6.25/93.75,v/v)	29.602	99.95%
MAF-X10(F)	C_2H_6/C_2H_4 (50/50,v/v)	22.044	99.95%

	C_2H_6/C_2H_4 (10/90,v/v)	43.965	99.95%
	C_2H_6/C_2H_4 (6.25/93.75,v/v)	47.874	99.95%

References

[1] R. Krishna, The Maxwell-Stefan Description of Mixture Diffusion in Nanoporous Crystalline Materials. Microporous Mesoporous Mater.185 (2014) 30-50.

[2] R. Krishna, Methodologies for Evaluation of Metal-Organic Frameworks in Separation Applications. RSC Adv. 5 (2019) 52269-52295.

[3] R. Krishna, Screening Metal-Organic Frameworks for Mixture Separations in Fixed-Bed Adsorbers using a Combined Selectivity/Capacity Metric. RSC Adv. 7 (2017) 35724-35737.

[4] R. Krishna, Methodologies for Screening and Selection of Crystalline Microporous Materials in Mixture Separations. Sep. Purif. Technol. 194 (2018) 281-300.

[5] R. Krishna, Metrics for Evaluation and Screening of Metal-Organic Frameworks for Applications in Mixture Separations. ACS Omega 5 (2020) 16987-17004.

[6] R. Krishna, Synergistic and Antisynergistic Intracrystalline Diffusional Influences on Mixture Separations in Fixed Bed Adsorbers. Precision Chemistry 1 (2023) 83-93.

[7] U. Böhme, B. Barth, C. Paula, A. Kuhnt, W. Schwieger, A. Mundstock, J. Caro and M. Hartmann, Ethene/Ethane and Propene/Propane Separation via the Olefin and Paraffin Selective Metal-Organic Framework Adsorbents CPO-27 and ZIF-8, Langmuir 29 (2013) 8592-8600.

[8] Y. Wang, C. Hao, W. Fan, M. Fu, X. Wang, Z. Wang, L. Zhu, Y. Li, X. Lu, F. Dai, Z. Kang, R. Wang, W. Guo, S. Hu, and D. Sun, One-step Ethylene Purification from an Acetylene/Ethylene/Ethane Ternary Mixture by Cyclopentadiene Cobalt-Functionalized Metal-Organic Frameworks, Angew. Chem. Int. Ed. 60 (2021) 11350-11358.

[9] X.-W. Gu, J.-X. Wang, E. Wu, H. Wu, W. Zhou, G. Qian, B. Chen, and B. Li, Immobilization of Lewis Basic Sites into a Stable Ethane-Selective MOF Enabling One-Step Separation of Ethylene from a Ternary Mixture, J. Am. Chem. Soc. 144 (2022) 2614-2623.

[10] X.-W. Gu, J. Pei, K. Shao, H.-M. Wen, B. Li, and G. Qian, Chemically Stable Hafnium-Based Metal-Organic Framework for Highly Efficient C_2H_6/C_2H_4 Separation under Humid Conditions, ACS Appl. Mater. Interfaces. 13 (2021) 18792-18799.

[11] G.-D. Wang, R. Krishna, Y.-Z. Li, W.-J. Shi, L. Hou, Y.-Y. Wang, and Z. Zhu, Boosting Ethane/Ethylene Separation by MOFs through the Amino-Functionalization of Pores, Angew. Chem. Int. Ed. 2022 (61) e202213015.

[12] W. Liang, F. Xu, X. Zhou, J. Xiao, Q. Xia, Y. Li, Z. Li, Ethane selective adsorbent $Ni(bdc)(ted)_{0.5}$ with high uptake and its significance in adsorption separation of ethane and ethylene, Chem. Eng. Sci. 148 (2016) 275-281.

[13] Y. Chen, Z. Qiao, H. Wu, D. Lv, R. Shi, Q. Xia, J. Zhou, Z. Li, An ethane-trapping MOF PCN-250 for highly selective adsorption of ethane over ethylene, Chem. Eng. Sci. 175 (2018) 110-117.

[14] O. T. Qazvini, R. Babarao, Z.-L. Shi, Y.-B. Zhang, and S. G. Telfer, A Robust Ethane-Trapping Metal-Organic Framework with a High Capacity for Ethylene Purification, J. Am. Chem. Soc. 2019, 141, 5014-5020.

[15] F. Jin, E. Lin, T. Wang, S. Geng, T. Wang, W. Liu, F. Xiong, Z. Wang, Y. Chen, P. Cheng, and Z. Zhang, Bottom-Up Synthesis of 8-Connected Three-Dimensional Covalent Organic Frameworks for Highly Efficient Ethylene/Ethane Separation, J. Am. Chem. Soc. 2022, 144, 5643-5652.

[16] K. Su, W. Wang, S. Du, C. Ji, D. Yuan, Efficient ethylene purification by a robust ethane-trapping porous organic cage, Nat Commun 12 (2021) 3703.

[17] H. Yang, Y. Wang, R. Krishna, X. Jia, Y. Wang, A. N. Hong, C. Dang, H. E. Castillo, X. Bu, and P. Feng, Pore-Space-Partition-Enabled Exceptional Ethane Uptake and Ethane-Selective Ethane-Ethylene Separation, J. Am. Chem. Soc. 142 (2020) 2222-2227.

[18] H. Zeng, X.-J. Xie, M. Xie, Y.-L. Huang, D. Luo, T. Wang, Y. Zhao, W. Lu, and D. Li, Cage-Interconnected Metal-Organic Framework with Tailored Apertures for Efficient C_2H_6/C_2H_4 Separation under Humid Conditions, J. Am. Chem. Soc. 141 (2019) 20390-20396.

[19] P.-Q. Liao, W.-X. Zhang, J.-P. Zhang and X.-M. Chen, Efficient purification of ethene by an ethane-trapping metal-organic framework, Nat. Commun. 6 (2015) 8697.

[20] L. Li, R.-B. Lin, R. Krishna, H. Li, S. Xiang, H. Wu, J. Li, W. Zhou, B. Chen, Ethane/ethylene separation in a metal-organic framework with iron-peroxo sites, Science 362 (2018) 443-446.

[21] X.-J. Xie, Y. Wang, Q.-Y. Cao, R. Krishna, H. Zeng, W. Lu and D. Li, Surface engineering on a microporous metal-organic framework to boost ethane/ethylene separation under humid conditions, Chem. Sci. 14 (2023) 11890-11895.

[22] Y. Zhou, C. Chen, R. Krishna, Z. Ji, D. Yuan, M. Wu, Tuning Pore Polarization to Boost Ethane/Ethylene Separation Performance in Hydrogen-Bonded Organic Frameworks, Angew. Chem. Int. Ed. 62 (2023) e202305041.

[23] Z. Xu, X. Xiong, J. Xiong, R. Krishna, L. Li, Y. Fan, F. Luo, B. Chen, A robust Th-azole framework for highly efficient purification of C_2H_4 from a $C_2H_4/C_2H_2/C_2H_6$ mixture, Nat. Commun. 11 (2020) 3163.